

# From Semiconducting to Metallic: Jahn–Teller-Induced Phase Transformation in Skyrmion Host $\text{GaV}_4\text{S}_8$

Yuejian Wang,\* Saqib Rahman, Elaine Sun, Christopher Knill, Dongzhou Zhang, Lin Wang, Vladimir Tsurkan, and István Kézsmárki



Cite This: *J. Phys. Chem. C* 2021, 125, 5771–5780



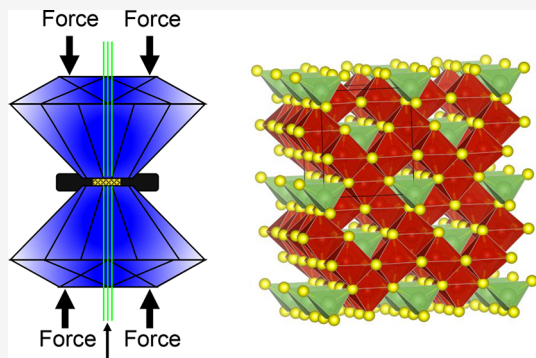
Read Online

ACCESS |

Metrics & More

Article Recommendations

**ABSTRACT:** Lacunar spinels,  $\text{GaM}_4\text{X}_8$  ( $\text{M} = \text{V}, \text{Nb}, \text{Mo}, \text{Ta}, \text{W}; \text{X} = \text{S}, \text{Se}, \text{Te}$ ), constitute a rare class of compounds with multiferroic properties. Recently, one member of this family,  $\text{GaV}_4\text{S}_8$ , received global attention due to the Néel-type skyrmions discovered in this material. Previous investigations strongly indicate the important role of the structure behind the multiferroicity, for example, the strong impact of ferroelectric transition on the exchange interactions at  $\sim 40$  K. Inspired by the delicate entanglement of lattice, spin, and charge degrees of freedom, in the present work, we aimed to use pressure to alter the structure and thus change the material's properties to establish the inter-relation between the structural, optical, and electrical properties for a better understanding of this skyrmion host material. Upon this objective, *in situ* high-pressure measurements of single crystal/powder X-ray diffraction, electrical conductivity, and Raman spectroscopy were carried out by using a diamond anvil cell. These studies revealed the pressure-induced structural transformation from cubic to orthorhombic, along with a transition from semiconductor to metallic state in  $\text{GaV}_4\text{S}_8$ . The phase changes coincide with the variation in the optical property in this material explored by Raman spectra. We also determined the bulk modulus of the two phases of  $\text{GaV}_4\text{S}_8$  by fitting the data set of unit cell volumes against pressure with the second-order birth-Murnaghan equation of state, and explained the mechanisms of phase transitions by means of the Jahn–Teller effect and the anisotropic changes in bonding lengths during compression.



## INTRODUCTION

$\text{GaV}_4\text{S}_8$  is one of the most popular materials in multi-disciplinary research fields, including condensed matter physics, chemistry, and materials science, mostly because of its unique electromagnetic properties.<sup>1–7</sup> For instance, in recent years, for the first time, the skyrmion lattice (SKL) was detected in  $\text{GaV}_4\text{S}_8$ , a polar crystal with a  $C_{3v}$  symmetry. This experimental discovery triggered considerable worldwide attention, although this phenomenon had been theoretically predicted three decades ago.<sup>2,8,9</sup> The exceptional nature of SKL is its periodic spin vortex array. The orientation of the vortices in SKL is anisotropic and energetically favorable to align with the magnetic easy axis.<sup>8,9</sup> Briefly, there are two types of SKL: Bloch and Neel. In a Bloch-type SKL domain, the rotation of spins is within the tangential planes, which are perpendicular to the radial directions; that is, the whirlpools of the spins are parallel to the domain wall of SKL. In contrast, in Neel-type SKL, spins rotate toward the periphery from the core along the radial direction. The Bloch-type SKL has been observed in a number of magnetic materials with chiral symmetry.<sup>10–20</sup> However, so far, the Neel-type SKL was experimentally observed only in  $\text{GaV}_4\text{S}_8$ , representing a

breakthrough in strong correlated systems.<sup>2</sup> The broad range of survival temperature along with the little dependence of its vortices orientation on the external magnetic field makes SKL robustly useful in many high technologies. For example, magnetic skyrmion may have an extraordinary capability to store information for the memory gadget and logic device as well as to provide a solution to the challenges faced in the racetrack-type-in-memory logic computing technologies.<sup>21–24</sup>

$\text{GaV}_4\text{S}_8$  is a representative member of the family of the lacunar spinel compounds with a generic chemical formula of  $\text{AM}_4\text{X}_8$ , in which  $\text{A} = \text{Ga}$  and  $\text{Ge}$  and  $\text{M} = \text{V}, \text{Mo}, \text{Nb}$ , and  $\text{Ta}$ , along with  $\text{X} = \text{S}$  and  $\text{Se}$ .<sup>2,4</sup> This family of structures can be obtained by the removal of every second  $\text{A}$  cation in the conventional spinel system. The cation deficiency alters the bonding and structure, shifting the  $\text{M}$  atoms off the center of

Received: November 23, 2020

Revised: February 12, 2021

Published: March 3, 2021



the  $\text{MX}_6$  octahedral and thus arranging the ions into a network consisting of two kinds of molecular units: tetrahedral  $\text{AX}_4$  and cubane  $\text{M}_4\text{X}_4$  cluster. Under ambient pressure and temperature conditions,  $\text{GaV}_4\text{S}_8$  crystallizes in a face-centered cubic structure (space group:  $F\bar{4}3m$ , No. 216,  $Z = 4$ ), as shown in Figure 1. A previous measurement and computation revealed

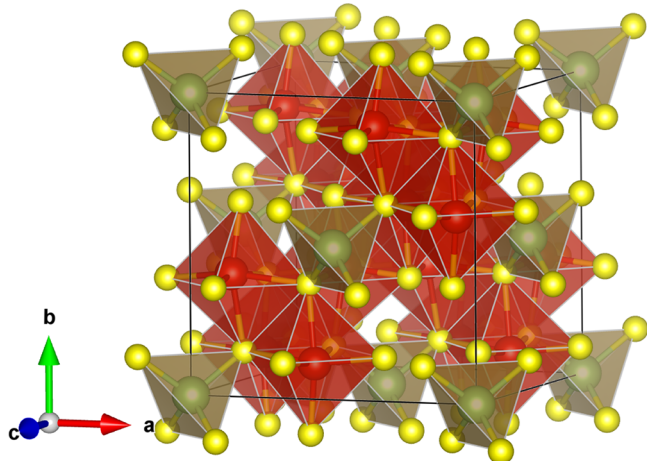


**Figure 1.** Visualization of the cubic phase of  $\text{GaV}_4\text{S}_8$ , including two polyhedrals,  $\text{VS}_6$  and  $\text{GaS}_4$ , in which green, red, and yellow balls represent the atoms of Ga, V, and S, respectively.

that under low temperature the original cubic  $\text{GaV}_4\text{S}_8$  distorts into a rhombohedral structure (space group:  $R\bar{3}m$ ; No. 160; formula units  $Z = 3$ ) at  $\sim 40$  K.<sup>4,5</sup> This structural transformation is regarded as a Jahn–Teller (JT) transition accompanied by an elongation of the tetrahedral  $\text{GaS}_4$  unit along the direction of  $\langle 111 \rangle$ , and the phase transition temperature,  $\sim 40$  K, is dubbed as  $T_{\text{JT}}$ . The onset of long-range magnetic ordering into a state with cycloidal spin arrangement is at 13 K.<sup>2</sup> Interestingly, the magnetic phases of  $\text{GaV}_4\text{S}_8$  depend on not only the temperature but also the externally applied magnetic field. Below 13 K, multiple phases, including regular ferromagnet, cycloidal, and Neel-type SKL, appear in the complex phase diagram of  $\text{GaV}_4\text{S}_8$ .<sup>2,3</sup> Under cooling from room temperature to 2 K, the material shows semiconducting behavior with a sudden drop of the electrical resistivity at  $T_{\text{JT}}$ .<sup>5,25</sup> Above  $T_{\text{JT}}$ , the electronic transport is dominated by the purely thermal activated behavior while, below  $T_{\text{JT}}$ , it is controlled by the variable range hopping or multielectron hopping.<sup>5,25</sup>

Like temperature, pressure is another controllable variable that can be externally altered to tune and probe the physical natures (lattice structure, optical, and electrical properties) of  $\text{GaV}_4\text{S}_8$  due to the strong coupling between lattice, electronic, and spin degrees of freedom in this compound.<sup>4</sup> More interesting, whether the Jahn–Teller effect, which has been observed in  $\text{GaV}_4\text{S}_8$  at the cooling condition as well as in  $\text{CuWO}_4$ ,  $\text{MnCr}_2\text{O}_4$ ,  $\text{NiCr}_2\text{O}_4$ , and  $\text{ZnCr}_2\text{S}_4$  under high pressure, is enabled to be induced by compression at room temperature in this compound.<sup>26–29</sup> However, the literature gives very limited information about the high-pressure behavior of  $\text{GaV}_4\text{S}_8$ .<sup>1,30</sup> Even its crystal structure transformation under room temperature compression is unknown. In the present study, we used high-pressure synchrotron single crystal and powder X-ray diffraction to detect the delicate change in the crystal structure of this material under a broad

pressure range from ambient to 60 GPa. We identify the crystal structure of the high-pressure phase and determine the compressibility of the bulk materials as well as the change in bonding lengths during the compression. Meanwhile, we conducted the high-pressure electrical resistance measurements at room temperature and elevated temperatures and, thus, construct the relation between the crystal structure transformation and the electrical phase transition. Furthermore, we carried out the Raman spectroscopic measurements under high pressure to complement the X-ray diffraction data. Overall, our study gives a complete scenario of the evolution of this compound under high pressure at room temperature, disclosing how its structure, electrical feature, and optical properties change under the influence from external compression.

## METHODS

The starting materials are  $\text{GaV}_4\text{S}_8$  single crystals and powders, respectively. Details of the sample synthesis have been reported elsewhere.<sup>31</sup> The high-pressure X-ray diffraction experiments were carried out by using a diamond anvil cell with a culet size of 300  $\mu\text{m}$ . Samples (powders or a single crystal) were loaded into a hole (working as the sample/pressure chamber) of 130  $\mu\text{m}$  in diameter and  $\sim 45$   $\mu\text{m}$  in depth drilled in the center of a rhenium gasket preindented by diamond anvils. A ruby crystal ( $< 15$   $\mu\text{m}$  in diameter) was also placed into the sample chamber for pressure calibration via using an online Ruby system.<sup>32</sup> To minimize the impact of strain/stress during measurements, the gas loading system at GSECARS of Argonne National Laboratory was used to fill argon gas, which served as the pressure-transmitting-medium (PTM), into the pressure chamber to attain a hydrostatic environment surrounding the sample.<sup>33–35</sup> The varied pressures were realized by utilizing a membrane system. We used synchrotron X-ray diffraction at the beamline 13-BM-C of Advanced Photon Source (APS) of Argonne National Laboratory to detect the changes in the powders and single crystal of  $\text{GaV}_4\text{S}_8$ , respectively, under high pressure up to 60 GPa. The incident monochromatic X-ray with a wavelength of 0.4340  $\text{\AA}$  was collimated to dimensions of about 12  $\mu\text{m}$  (horizontal)  $\times$  18  $\mu\text{m}$  (vertical), measured as the full width at half-maximum. A MAR345 image plate, placed 198 mm (powder diffraction) and 154 mm (single crystal diffraction) away from the sample, was used to collect the X-ray diffraction data, respectively. Those distances between the sample and the image plate and the tilting of the image plate were calibrated by using the ambient powder diffraction pattern of  $\text{LaB}_6$  collected at the same diffractometer prior to the departure of the high-pressure measurements. Dioptas was used to convert the powder diffraction Debye rings into conventional X-ray diffraction patterns,<sup>36</sup> which were then refined via the Rietveld refinement method using GSAS-II to obtain the lattice parameters and unit cell volume of  $\text{GaV}_4\text{S}_8$  at each pressure point.<sup>37</sup> In Rietveld refinement, the sample's diffraction background coming from the noncharacteristic emissions of the X-ray tube, air scattering, sample fluorescence, and so on, is treated by a Chebyshev Polynomial, and the peak width/shape is formulated by a so-called peak shape function, which is a convolution of three functions: the instrumental broadening, wavelength dispersion, and the specimen function.<sup>38</sup>

The data collecting and processing of single crystal diffraction data were somewhat different from those of powder diffraction data. Details have been reported elsewhere.<sup>39</sup> We

collected two types of single crystal X-ray data, wide-angle X-ray diffraction images and step diffraction images, at each pressure point. The wide-angle X-ray diffraction image covers  $46^\circ$ , the total axial opening angle of the DAC, with a single exposure time of 60 s, while the single image covers  $1^\circ$  with a 4 s exposure time. Therefore, at each pressure point, the total opening angle of  $46^\circ$  was scanned by consecutive 46 diffractions. Like the powder diffraction patterns, the wide-angle diffraction images were integrated into conventional X-ray profiles (intensity vs  $2\theta$  as well as intensity vs  $d$ -spacing).<sup>36</sup> We used ATREX/RSV software to determine the crystal structures of the high-pressure phase of the sample by analyzing the single crystal diffraction data.<sup>40</sup> The lattice parameters and the unit cell volume of the single crystal  $\text{GaV}_4\text{S}_8$  at each pressure point were calculated by using a program embedded in Microsoft Excel.<sup>41</sup> The representative visualization image of the crystal structure of  $\text{GaV}_4\text{S}_8$  was generated by using the software package of VESTA.<sup>42</sup>

An inVia Renishaw Raman system operated with a green laser (wavelength 512 nm) and a grating of 2400 g/cm was used to carry out the high-pressure Raman measurements. The pressure environment was generated by using a diamond anvil cell in which silicon oil served as the PTM.<sup>43,44</sup> The uncertainty of the measured pressure depends on the pressure applied onto the sample. The higher the pressure, the larger the uncertainty. In our measurements, using Ar and silicon oil, respectively, as the PTMs, the pressure uncertainty is about  $\sim 0.4$  GP up to 60 GPa. The uncertainty of the determination of the Raman spectroscopic peak is about  $1 \text{ cm}^{-1}$ . The high-pressure electrical resistivity was measured by using a standard four-probe system installed in a diamond anvil cell in which no PTA was employed.<sup>45,46</sup> The isolation between electrodes was realized by a layer of a mixture of epoxy and cubic boron nitride smeared on the surface of a steel gasket where the four-probe was mounted. The electrodes, which directly contact the sample, were made of platinum, and copper wires were used to connect the electrodes to a 4050 Keithley digital multimeter by which the voltage and current passing through the sample were probed, and thereafter, the resistances of the sample under pressure were calculated by the van der Pauw method.<sup>47</sup> We used single crystals of  $\text{GaV}_4\text{S}_8$  to perform the high-pressure Raman/electrical resistivity measurements.

## RESULTS AND DISCUSSION

The sample was compressed at room temperature by using a diamond anvil cell coupled with synchrotron X-ray, and the diffraction patterns are shown in Figure 2. The ambient pattern indicates that the starting material is pure  $\text{GaV}_4\text{S}_8$  without any detectable impurity. Furthermore, the X-ray data refinement suggests that at ambient conditions  $\text{GaV}_4\text{S}_8$  adopts a face-centered cubic structure,  $F\bar{4}3m$  space group (#216), with a lattice parameter of 9.665 Å, which is in good agreement with the previous studies.<sup>4,5,25</sup> With pressures increasing, the peaks of powder X-ray diffraction patterns gradually shift to the higher angle positions, since the external force squeezes atomic layers moving toward each other. Besides the peaks' shifts, the powder X-ray diffraction patterns do not show any abrupt changes until the pressure reached  $\sim 30$  GPa, where three new peaks located at  $\sim 5^\circ$ ,  $8^\circ$ , and  $10^\circ$  appear, as shown in Figure 2. It may suggest the starting of a phase transformation, and this process spans a wide range of pressure, from 29.4 GPa to 52.6, during which the sample is a mixture consisting of the starting and high-pressure phases. Above 55.6 GPa, the entire sample

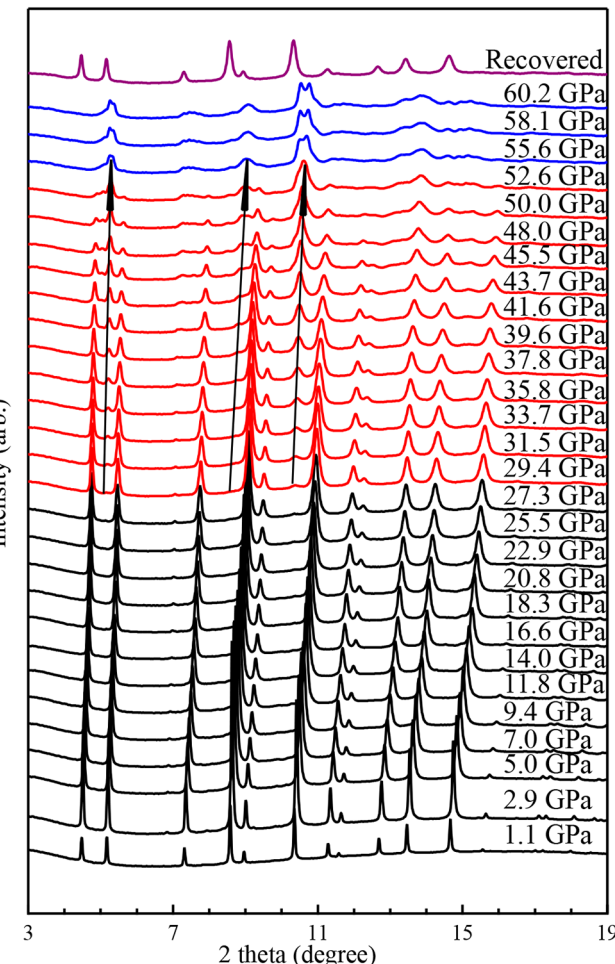


**Figure 2.** X-ray patterns of the sample under various pressures. Black, red, blue, and purple ones are the patterns of starting cubic phase, the mixture of the starting and high-pressure phases, and the pure high-pressure phase, and the recovered sample, respectively. The arrows denote the main Bragg peaks of the orthorhombic structure, a high-pressure phase of  $\text{GaV}_4\text{S}_8$ .

transforms into the high-pressure phase. The broad peaks, weak signals, plus the unsymmetrical peak shapes, suggest the disordered fine grains (even partially amorphized) in this high-pressure phase.

Up to 60.2 GPa, the high-pressure phase is well maintained without any transition. Meanwhile, the phase is unquenchable. As the pressure is released to the ambient conditions, it reverts to the starting structure. We also see the broad peaks in the recovered X-ray pattern compared to those from the starting materials, suggesting that after the high-pressure test, though the crystal structure goes back to the original one, the constituent grains in the recovered sample are much smaller.

To identify the high-pressure phase, a single crystal diffraction measurement was performed and the representative patterns are shown in Figure 3a,b. The diffraction pattern shows that at  $\sim 34$  GPa the starting cubic phase departs to transform to a new phase. This departure pressure is slightly higher than that determined from the powder diffraction, which may be due to the different sizes and morphologies of the constituent crystals in the samples as well as the distinct data processing approaches. The single crystal X-ray diffraction data provided solution to the crystal structure of the high-

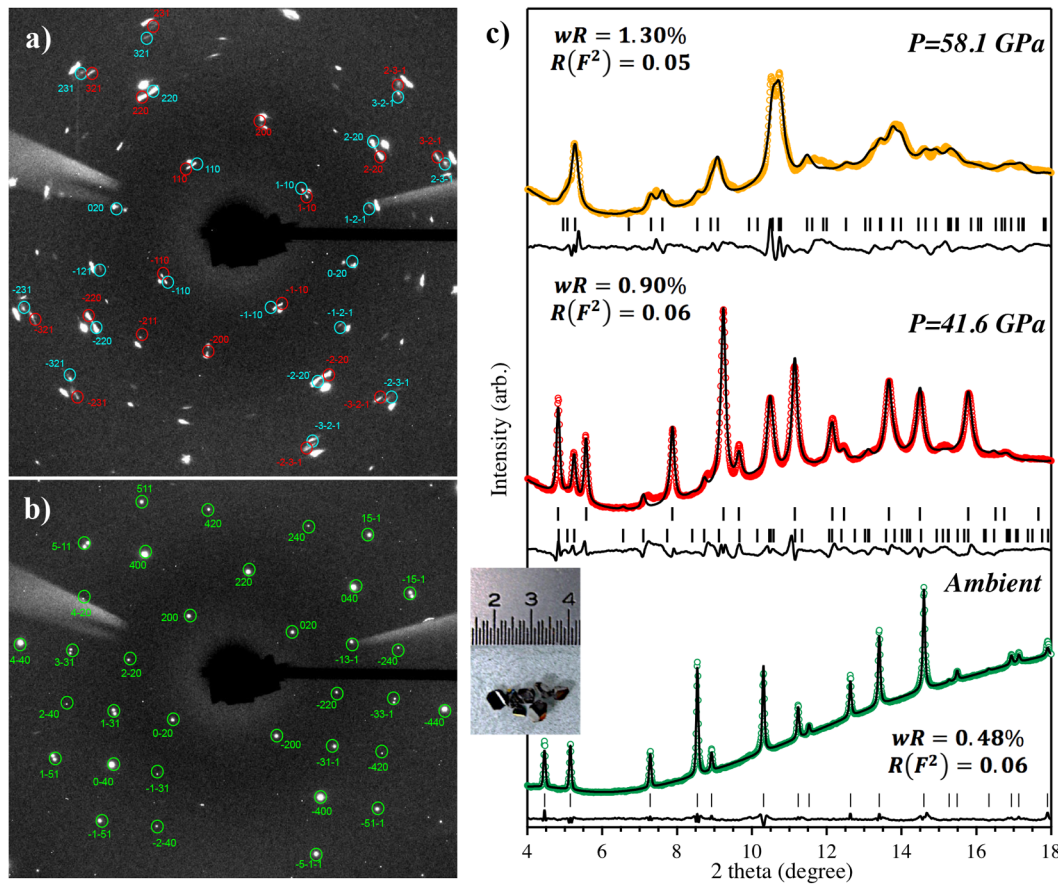


**Figure 3.** (a) The single crystal X-ray diffraction pattern at 43.2 GPa. The reflections are marked with circles, and due to the twinning, there are two sets of diffraction peaks, distinguished with different colors. (b) The single crystal diffraction pattern collected at ambient conditions. (c) The representative refinements of X-ray powder diffraction patterns collected at different pressures. The open circles represent the observed data, and the solid lines are the calculated patterns while the differences between observations and calculated results are depicted underneath the patterns. The peak positions are also illustrated with bars just above the difference curve. The ambient pattern is from the starting material with a cubic phase. The pattern collected at 41.6 GPa includes cubic plus orthorhombic phases. The pattern collected at 58.1 GPa is from the pure orthorhombic phase. Few tiny bumps in the diffraction patterns may come from the PTM of Ar. Inset: the image of crystals of the starting  $\text{GaV}_4\text{S}_8$ .

pressure phase, turning out that the high-pressure phase adopts an orthorhombic structure (space group  $\text{Imm}2$ , No. 44), which is the symmetry of  $\text{GeV}_4\text{S}_8$  at its low-temperature polar phase.<sup>25</sup> The crystallographic data are tabulated in Table 1. The high-pressure  $\text{Imm}2$  phase is a subgroup of the starting  $\bar{F}43m$  phase, and there is no coordination change whatsoever, so these two structures are very similar. The slight difference between these two structures lies in the lengths of the lattice sides: the cubic structure is the most symmetrical system with lattice parameters of  $a = b = c$  and  $\alpha = \beta = \gamma = 90^\circ$ , while in orthorhombic structure,  $\alpha$ ,  $\beta$ , and  $\gamma$  are equal to  $90^\circ$ , while all of its sides are not equal in length. Then we went back to process the powder X-ray diffraction patterns of the high-pressure phase by using this determined structure, resulting in refinements with very small uncertainties, as shown in Figure 3c.

The single crystal diffraction patterns maintain resolvable up to 47 GPa, beyond which the crystals crushed into powders, thus, preventing us from further doing the single crystal analysis. Therefore, our single crystal diffraction study on the high-pressure phase is limited to the pressure range of 34–47 GPa.

**Table 1. Crystallographic Data of the Starting and High-Pressure Phases of  $\text{GaV}_4\text{S}_8$**

space group	$\bar{F}43m$	$\text{Imm}2$
pressure	ambient	43.2 GPa
$a$ (Å)	8.985(1)	6.990(1)
$b$ (Å)		6.412
$c$ (Å)		7.500
$V$ (Å <sup>3</sup> )	725.36(1)	336.14(9)
atomic coordinates	Ga(1):4a [0,0,0] V(1):16e [0.6056(3),0.6056(3), 0.6056(3)] S(1):16e [0.3720(1),0.3720(1), 0.3720(1)] S(2):16e [0.8635(1),0.8635(1), 0.8635(1)]	Ga(1):2a [0,0,0] V(1):4d [0,0.2112(6), 0.6056(3)] V(2):4c [0.2112(6), 0,0.3943(7)] S(1):4d [0,0.7440(1), 0.3720(1)] S(11):4c [0.2560(1), 0,0.6280(1)] S(2):4d [0,0.7270(1), 0.8635(1)] S(21):4c [0.2730(1), 0,0.1365(1)]

We also calculated the bulk moduli of cubic and orthorhombic structures via fitting the  $P$ – $V$  data set to a second-order Birch–Murnaghan equation of state,<sup>48,49</sup>

$$P(V) = \frac{3B_0}{2} \left[ \left( \frac{V_0}{V} \right)^{7/3} - \left( \frac{V_0}{V} \right)^{5/3} \right]$$

Here  $B_0$  is the bulk modulus,  $V_0$  refers to the volume at ambient conditions, and  $V$  stands for the volume at a given pressure. In the present study, the derivative of the bulk modulus with respect to pressure is fixed to 4. The least-squares fitting, shown in Figure 4, yielded bulk moduli of 132

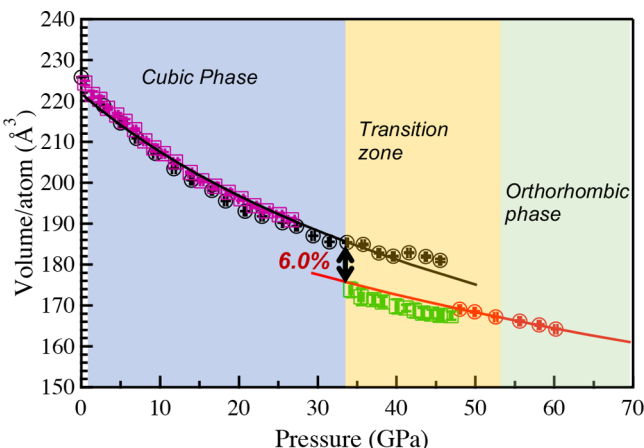


**Figure 4.** Volume occupied by individual atom versus pressure. The data from powder diffraction patterns are illustrated with open black and red circles while those from single crystal data are depicted with open purple and green squares. The error bars of the pressures and volumes are smaller than the symbols as presented in the figure. The solid curves represent the EOS fitting results (black color for cubic and red for orthorhombic phase). The phase transition is accompanied by a reduction in volume by ~6%.

$\pm 5$  and  $225 \pm 9$  GPa for cubic and orthorhombic phases, respectively, indicating that the high-pressure phase is stiffer than the cubic phase with a more than 70% increase in the bulk modulus. The errors in the fitting results come from the fitting process without including the propagation of uncertainties from pressure and volume. The bulk modulus of the cubic phase of this lacunar spinel compound is different from other conventional spinels, such as  $\text{ZnGa}_2\text{O}_4$ ,<sup>50</sup>  $\text{ZnCr}_2\text{Se}_4$ ,<sup>51</sup>  $\text{CoCr}_2\text{O}_4$ ,<sup>52</sup>  $\text{CuCr}_2\text{O}_4$ ,<sup>53</sup>  $\text{ZnCr}_2\text{S}_4$ ,<sup>28</sup>  $\text{MnCr}_2\text{O}_4$ ,<sup>27</sup>  $\text{NiCr}_2\text{O}_4$ ,<sup>27</sup>

$\text{CdCr}_2\text{Se}_4$ ,<sup>54</sup> and so on. The discrepancies are predominantly caused by the different crystal structures,  $F\bar{4}3m$  versus  $Fd\bar{3}m$ , in these two systems.

Raman spectroscopy is a useful approach to probe materials' optical characteristic and in turn may give us hints about the change in the electrical property under high pressure. Meanwhile, it provides information to complement the phase transition scenario derived from the X-ray diffraction data. Figure 5a shows the high-pressure Raman spectra collected from the crystal facet of (111) in  $\text{GaV}_4\text{S}_8$  at room temperature. According to group theory, 12 Raman active modes ( $3A_1$ ,  $3E$ , and  $6F_2$ ) are expected to be present in the spectra.<sup>6</sup> In the present study, at low pressures, five active modes are detected. The peak at  $\sim 410 \text{ cm}^{-1}$  contains two Raman modes of 404 and 411. As pressure increases, these two modes become resolvable due to their different pressure sensitivities. Though both shift to higher wavenumbers as pressure increases, the 411 mode moves faster, so at pressures above 5.3 GPa, these two peaks clearly split. In the entire pressure range, we did not observe any new mode emerging or existing mode suddenly vanishing, but we saw that the intensities of the signals decrease gradually with pressures compared to the background scattering and become totally featureless at 34.3 GPa. Meanwhile, we observed the different sensitivities of the Raman modes to the pressure. The wavenumber of one of the  $F_2$  modes, located at  $134 \text{ cm}^{-1}$  at 1.2 GPa, decreases with pressure up to the disappearance of the Raman signature. This soft mode, the searched Jahn–Teller active band, may be linked to the distortion/translation of cubane  $\text{V}_4\text{S}_4$  unit relative to the Ga atom.<sup>55</sup> In contrast, all of the other modes hardened upon compression. The disappearance of the soft mode is a key indicator for the occurrence of a phase transition in a material, which has been observed in other systems.<sup>56</sup> All of the evidence from X-ray and Raman measurements suggest that the pressure induced crystal structural transformation is perhaps accompanied by the change in the electrical property of  $\text{GaV}_4\text{S}_8$ .

However, it has to be verified by the electrical conductivity measurements. Since there is a phase transition, the further question is at which pressure this transition starts? Because the Raman spectra do not abruptly change under pressure, also considering that high-pressure induced thinning of the sample inherently gives rise to the weak signals in addition to the

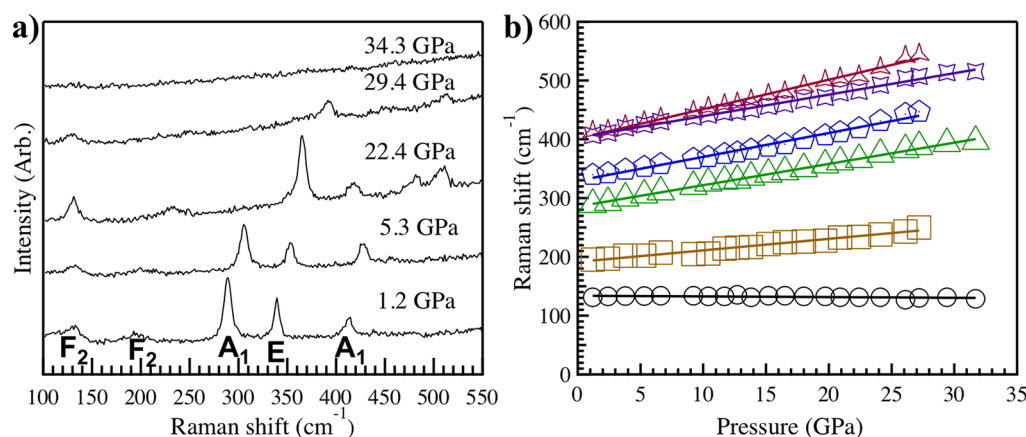


**Figure 5.** (a) Raman spectra collected at various pressures. At 29.4 GPa, the intensities of Raman modes abruptly decrease, which may indicate the departure of phase transition. At 34.3 GPa, all of the peaks disappear, suggesting the new phase is a conducting material. (b) Peak positions of Raman modes against pressures. The straight lines represent the linear data fitting.

phase transition, it is difficult to accurately determine the departure pressure. Nevertheless, if focusing on the higher Raman shift region in the Raman spectra, one may find that at  $\sim 29.4$  GPa, the intensities of three bands (tracing back to 336, 404, and 411 at the ambient conditions) decreases severely compared to other lower pressure spectra. So, this mode weakening may indicate the crystal structural transformation is accompanied by the presence of a strongly anharmonic potential energy for atomic displacement.<sup>57</sup> The pressure determined here, 29.4 GPa, is consistent well with the one for the transition from cubic to orthorhombic demonstrated in the X-ray diffraction data. Though the silicon oil and Ar were used as PTAs for the X-ray diffraction and Raman measurements,<sup>34</sup> respectively, the quite similar hydrostatic conditions generated by them surrounding the sample under compression further support our conclusion that the transformation detected by X-ray diffraction and the one probed by Raman measurement are most likely coincident. We also calculated the pressure coefficients,  $d\omega/dP$ , by fitting the data of Raman peak position versus pressure, as shown in Figure 5b. The pressure coefficients of this material are much larger (almost doubled) than another nano spinel  $\text{CoFe}_2\text{O}_4$ .<sup>58</sup> These discrepancies may be attributed to the different crystal structures and the dimensions (single crystal for the present study vs nanosizes of  $\text{CoFe}_2\text{O}_4$ ) of the constituent crystallites between these two materials. Based on the pressure coefficients and the bulk modulus,  $B_0$ , determined from X-ray diffraction study, the Grüneisen parameters ( $\gamma$ ) for each mode was calculated by using equation  $\gamma = \frac{B_0}{\omega_0} \left( \frac{d\omega}{dP} \right)$ , where  $\omega_0$  is the wavenumber of the phonon mode at the ambient conditions. Because single crystal was adopted for the Raman measurements, here we used the bulk modulus, 116.3 GPa, of single crystal for the calculation. Among the values of  $\gamma$ , as listed in Table 2, one of

**Table 2.** Raman Band, Band Frequency at the Ambient Condition, and Grüneisen Parameters for the Cubic Phase of  $\text{GaV}_4\text{S}_8$ ; The Estimated Uncertainty for  $\frac{d\omega}{dP}$  is about 0.01 ( $\frac{\text{cm}^{-1}}{\text{GPa}}$ )

band	$\omega_0$ ( $\text{cm}^{-1}$ )	$d\omega/dP$ ( $\text{cm}^{-1}/\text{GPa}$ )	$\gamma$
$F_2$	134(1)	-0.1	-0.11(S)
$F_2$	191(1)	2.0	1.19(S)
$A_1$	286(1)	3.6	1.48(S)
$E$	330(1)	4.1	1.44(S)
$A_1$	403(1)	3.6	1.05(S)
$A_1$	402(1)	5.0	1.45(S)

the  $F_2$  bands has a negative number, while all others are positive ranging from  $\sim 2$  to 5. These results are consistent with our observation that the modes located at higher wavenumber positions shift faster with the pressure increasing. It suggests the anisotropic effect of the volume changes, as observed from the X-ray measurements, induced by external stress on the photons' dynamics. These values are critical for the determination of other physical properties, such as heat capacities and vibrational entropy.

To supplement the X-ray diffraction and Raman study, we also measured the change in the electrical resistance of a single-crystalline  $\text{GaV}_4\text{S}_8$  under high pressure at room temperature, as shown in Figure 6a. At ambient conditions, the resistivity of  $\text{GaV}_4\text{S}_8$  is  $\sim 240 \Omega\cdot\text{cm}$ , suggesting that the starting material is a

semiconductor, and the similar electrical property has been observed in several ternary chalcogenides.<sup>4,5,57</sup> As pressure increases, the resistivity decreases almost linearly, indicating more charge carriers have gained sufficient energy from external compression and thus enabled to cross the band gap thereby enhancing the conductivity of the material, and the same behavior also detected in  $\text{GaNb}_4\text{Se}_8$ ,  $\text{GaTa}_4\text{Se}_8$ , and  $\text{Cd}_{0.90}\text{Zn}_{0.1}\text{Te}$ .<sup>57,59</sup> Starting from  $\sim 15$  GPa (point A in Figure 6a), the dropping in resistivity slows down up to  $\sim 40$  GPa (point B in Figure 6a), beyond which the resistivity is independent of the pressure and the low resistivity suggests that the bandgap reaches zero and the material fully transits into a conductor from a semiconductor. A recent study detected that  $\text{GaV}_4\text{S}_8$  completely transforms into a conductor at  $\sim 12$  GPa, which is lower than our result here.<sup>30</sup> Additionally, the present investigation determined the pressure range, 15–40 GPa, during which the electrical phase transformation takes place. Comparing with the crystal structural transformation determined from the X-ray data, we seemingly saw a decoupling between these two transformations. First of all, the transition pressure ranges are somewhat different, 30–53 GPa for crystal structural transformation versus 15–40 GPa for electrical phase transition, though there exists an overlapping portion. Second, the cubic phase exhibits subsequently semiconducting and conducting characteristics depending on the externally applied pressure while the orthorhombic structure only demonstrates the conducting behavior. However, concerning the relatively large deviatoric stresses developed across the sample under compression during the electrical resistivity measurement, compared to X-ray diffraction and Raman experiments, the discrepancies among the departure pressures determined by these three measurements perhaps are not so significant.

To scrutinize the metallization of  $\text{GaV}_4\text{S}_8$  under high pressure, we investigated the relationship between its resistivity and temperature at five respective pressures, 2.0, 11.0, 19.0, 29.5, and 38 GPa. Under a given pressure as the sample was heated from room temperature up to 420 K, the resistivity was measured at each temperature point. As shown in Figure 6b, when the pressure value is smaller than 29.5 GPa, we see a negative slope of resistivity versus temperature, while at 29.5 GPa, the sample's resistivity seems almost independent of the temperature. Upon further increasing pressure to 38 GPa, we observed a slight increase in the resistivity with temperature. This evolution of the sample's resistivity with temperature under given respective different pressures suggests that the metallization in  $\text{GaV}_4\text{S}_8$  takes place at  $\sim 29.5$  GPa. Above this pressure point, like a regular metal, the resistivity of  $\text{GaV}_4\text{S}_8$  increases with temperature due to the elevated thermal ions' vibrations restricting the movement of delocalized electrons. At a pressure below 29 GPa, the material behaves like a nonmetal conductor. Upon temperature increasing, electrons become more energetic due to the thermal energy injection externally and thus more electrons participate in electrical transportation. Therefore, we observe a negative slope in the curve of resistivity versus temperature below 29 GPa. This mechanism also can be used to explain the resistivity drops with pressure at room temperature, as shown in Figure 6a, the only difference is that the electrons inside the sample gain energy from the external environment by a means of compression instead of heating. Overall,  $\text{GaV}_4\text{S}_8$  is a semiconductor at ambient pressure and temperature conditions. As pressure increases,

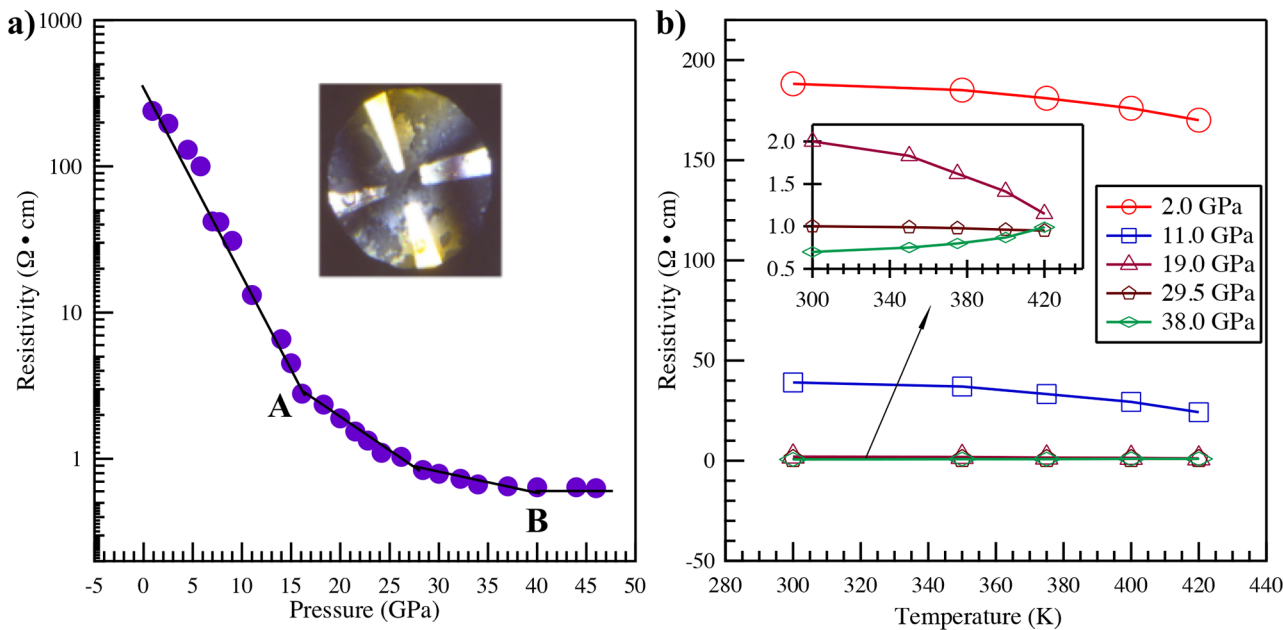


**Figure 6.** Evolution of the sample's resistivity under pressure and temperature. (a) Resistivity vs pressure at room temperature. Inset: the image of diamond anvil installed with the electrodes. (b) Resistivity vs temperature for five pressure points.

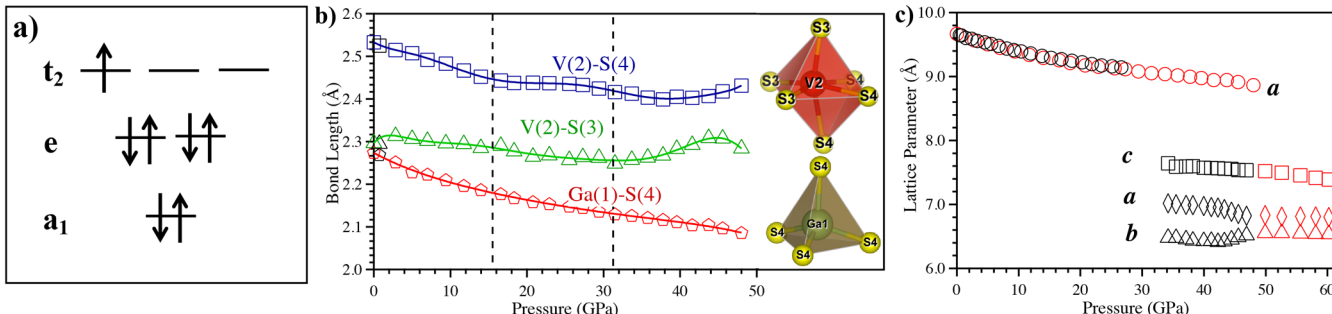


**Figure 7.** (a) Electronic configuration of d-orbitals in  $\text{V}_4\text{S}_4$  cluster at ambient pressure. (b) Bond lengths vs pressure for cubic phase. The insets are the units of  $\text{VS}_6$  (top) and  $\text{GaS}_4$  (bottom). (c) Lattice parameters versus pressure for cubic phase (open circles) and orthorhombic phase (squares, diamonds, and triangles) from powder diffraction data (red) and single crystal data (black).

the material transforms into a nonmetal conductor and then metallic material.

Reminded by the Jahn–Teller effect during the transition from cubic to rhombohedral phase at low temperature and ambient pressure,<sup>55</sup> we closely checked the changes in bonding length, lattice parameters as well as the local electronic state under pressure, as shown in Figure 7, to find the mechanism for the cubic to orthorhombic transition accompanied by the electrical transformation from semiconductor to metallic material. As stated in the Introduction section, the V atom shifts off the center of  $\text{VS}_6$  octahedron, which generates the localized electronic structure in the  $\text{V}_4\text{S}_4$  cluster and thus leading to the entire material's unique magnetic and transport properties.<sup>5</sup> According to the molecular orbital (MO) calculation, the localized electronic structure consists of three d-orbitals in  $\text{V}_4\text{S}_4$  cluster, namely,  $a_1$  (nondegenerate),  $e$  (2-fold degenerated energy level), and  $t_2$  (3-fold degenerated level), as shown in the MO scheme, Figure 7a.<sup>26</sup> Among them,  $t_2$  is the highest energy level. These three bonding states can be completely filled with 12 electrons, while, in the case of  $\text{GaV}_4\text{S}_8$ , only seven electrons are accommodated with two, four, and one electron in  $a_1$ ,  $e$ , and  $t_2$  bonding orbitals,

respectively. These bonding structures change with pressures, as shown in Figure 7b. At the beginning of the compression, both bond lengths of  $\text{V}(2)-\text{S}(4)$  within the  $\text{V}_4\text{S}_4$  cluster and  $\text{V}(2)-\text{S}(3)$  bridging the  $\text{V}_4\text{S}_4$  clusters decrease. However, after  $\sim 15$  GPa, the bond of  $\text{V}(2)-\text{S}(3)$  continues to shorten whereas that of  $\text{V}(2)-\text{S}(4)$  remains almost the same, suggesting that compression induces the V atom to move toward the center of  $\text{VS}_6$  octahedra. This movement leads to a decrease of the distortion of octahedra, and thereby an increase of the hybridization of d-orbital in  $\text{V}_4\text{S}_4$  cluster which may result in the enhancement of the hopping effect, as reflected by the substantial drop of electrical resistivity. From  $\sim 31$  GPa, the bonds start to lengthen with pressure instead of shortening. This distortion may be correlated with the crystal structure phase transition confirmed by the appearance of new peaks at  $\sim 30.0$  GPa, as shown in Figure 2.

As expected, lattice shortens continuously in the cubic phase with pressures. However, in the orthorhombic phase, lattices demonstrate anisotropic changes during the phase transition. Lattice parameters  $a$  and  $c$  shorten, but  $b$  elongates as pressure increases. Beyond the phase transition zone, in the orthorhombic structure, the lattice  $c$  shortens gradually and

smoothly as pressure increases, but the lattices *a* and *b* are almost independent of the pressure, as demonstrated in Figure 7c. Therefore, lattice *c* is a soft direction along which the unit cells are largely squeezed while almost unchanged along *a* and *b* directions. This geometrical distortion generating the Jahn–Teller effect may alter the degenerate electronic state in V<sub>4</sub>S<sub>4</sub> cluster, tending to lower the global energy of crystals by means of removing the degeneracy (for example, split the 3-fold degenerated t<sub>2</sub> levels into nondegenerated level).

## CONCLUSIONS

In summary, GaV<sub>4</sub>S<sub>8</sub> reveals a transition from cubic to orthorhombic structure under high pressure determined by both single crystal and powder X-ray diffractions. This transition is sluggish lasting a wide pressure range from 31.5 to 52.6 GPa. We also found that the high-pressure phase with an orthorhombic structure is stiffer than the starting cubic phase. The supplementary high-pressure Raman measurements verified the phase transition observed in the X-ray diffraction, and also gave us a hint about the electrical property of the orthorhombic phase. Furthermore, the electrical conductivity experiments demonstrated that under high pressure GaV<sub>4</sub>S<sub>8</sub> transforms from the starting semiconductor into a nonmetallic conductor and then into a metallic material. We attempted to explain the mechanism behind the transition by scrutinizing the lattice parameters and bond lengths under pressure. We proposed that the phase transformations under pressure may be induced by the Jahn–Teller effect which removes the degeneracy of the 3-fold degenerated t<sub>2</sub> level.

## AUTHOR INFORMATION

### Corresponding Author

**Yuejian Wang** — Physics Department, Oakland University, Rochester, Michigan 48309, United States;  [orcid.org/0000-0001-6663-5912](https://orcid.org/0000-0001-6663-5912); Email: [ywang235@oakland.edu](mailto:ywang235@oakland.edu)

### Authors

**Saqib Rahman** — Center for High-Pressure Science and Technology Advanced Research, Beijing 100094, China

**Elaine Sun** — GSECARS, University of Chicago, Argonne, Illinois 60439, United States

**Christopher Knill** — Physics Department, Oakland University, Rochester, Michigan 48309, United States

**Dongzhou Zhang** — Partnership for Extreme Crystallography, University of Hawaii at Manoa, Honolulu, Hawaii 96822, United States;  [orcid.org/0000-0002-6679-892X](https://orcid.org/0000-0002-6679-892X)

**Lin Wang** — Center for High-Pressure Science (CHIPS), State Key Laboratory of Metastable Materials Science and Technology, Yanshan University, Qinhuangdao, Hebei 066004, China;  [orcid.org/0000-0003-2931-7629](https://orcid.org/0000-0003-2931-7629)

**Vladimir Tsurkan** — EP V, Center for Electronic Correlations and Magnetism, University of Augsburg, 86159 Augsburg, Germany; Institute of Applied Physics, MD-2028 Chisinau, Republic of Moldova

**István Kézsmárki** — EP V, Center for Electronic Correlations and Magnetism, University of Augsburg, 86159 Augsburg, Germany

Complete contact information is available at:

<https://pubs.acs.org/10.1021/acs.jpcc.0c10527>

### Notes

The authors declare no competing financial interest.

## ACKNOWLEDGMENTS

We would like to thank Dr. S. Tkachev at GeoSoilEnviroCARS (Sector 13), APS-ANL for his assistance with the DAC gas loading. Portions of this work were performed at GeoSoilEnviroCARS (The University of Chicago, Sector 13), APS, Argonne National Laboratory. GeoSoilEnviroCARS is supported by the National Science Foundation - Earth Sciences (Grant No. EAR-1128799) and Department of Energy - GeoSciences (Grant No. DE-FG02-94ER14466). This research used resources of the Advanced Photon Source, a U.S. DOE Office of Science User Facility operated for the DOE Office of Science by Argonne National Laboratory under Contract No. DE-AC02-06CH11357. Use of the COMPRES-GSECARS gas-loading system was supported by COMPRES under NSF Cooperative Agreement No. EAR 11-57758 and by GSECARS through NSF Grant No. EAR-1128799 and DOE Grant No. DE-FG02-94ER14466. This research used resources of the Advanced Photon Source, a U.S. DOE Office of Science User Facility operated for the DOE Office of Science by Argonne National Laboratory under Contract No. DE-AC0206CH11357. This work was also partially supported by the Transregional Research Collaboration TRR 80 (Augsburg, Munich, and Stuttgart) and by Institutional Project 15.817.02.06F (Moldova). We are grateful to the Faculty Research Grant from Oakland University for supporting this research.

## REFERENCES

- (1) Nii, Y.; Nakajima, T.; Kikkawa, A.; Yamasaki, Y.; Ohishi, K.; Suzuki, J.; Taguchi, Y.; Arima, T.; Tokura, Y.; Iwasa, Y. Uniaxial Stress Control of Skyrmion Phase. *Nat. Commun.* **2015**, *6*, 8539.
- (2) Kézsmárki, I.; Bordács, S.; Milde, P.; Neuber, E.; Eng, L. M.; White, J. S.; Rønnow, H. M.; Dewhurst, C. D.; Mochizuki, M.; Yanai, K.; et al. Néel-Type Skyrmion Lattice with Confined Orientation in the Polar Magnetic Semiconductor Gav4s8. *Nat. Mater.* **2015**, *14*, 1116–1122.
- (3) Ruff, E.; Widmann, S.; Lunkenheimer, P.; Tsurkan, V.; Bordács, S.; Kézsmárki, I.; Loidl, A. Multiferroicity and Skyrmions Carrying Electric Polarization in Gav4s8. *Sci. Adv.* **2015**, *1*, e1500916.
- (4) Müller, H.; Kockelmann, W.; Johrendt, D. The Magnetic Structure and Electronic Ground States of Mott Insulators Gev4s8 and Gav4s8. *Chem. Mater.* **2006**, *18*, 2174–2180.
- (5) Pocha, R.; Johrendt, D.; Pöttgen, R. Electronic and Structural Instabilities in Gav4s8 and Gamo4s8. *Chem. Mater.* **2000**, *12*, 2882–2887.
- (6) Hlinka, J.; Borodavka, F.; Rafalovskyi, I.; Docekalova, Z.; Pokorny, J.; Gregora, I.; Tsurkan, V.; Nakamura, H.; Mayr, F.; Kuntscher, C. A.; et al. Lattice Modes and the Jahn-Teller Ferroelectric Transition of Gav4s8. *Phys. Rev. B* **2016**, *94*, 060104.
- (7) Ehlers, D.; Stasinopoulos, I.; Kézsmárki, I.; Fehér, T.; Tsurkan, V.; Nidda, H.-A. K. v.; Grundler, D.; Loidl, A. Exchange Anisotropy in the Skyrmion Host Gav4s8. *J. Phys.: Condens. Matter* **2017**, *29*, 065803.
- (8) Bogdanov, A. N.; Hubert, A. Thermodynamically Stable Magnetic Vortex States in Magnetic Crystals. *J. Magn. Magn. Mater.* **1994**, *138*, 255–269.
- (9) Bocdanov, A. N.; Hubert, A. The Properties of Isolated Magnetic Vortices. *Phys. Status Solidi B* **1994**, *186*, 527–543.
- (10) Mühlbauer, S.; Binz, B.; Jonietz, F.; Pfleiderer, C.; Rosch, A.; Neubauer, A.; Georgii, R.; Böni, P. Skyrmion Lattice in a Chiral Magnet. *Science* **2009**, *323*, 915–919.
- (11) Yu, X. Z.; Kanazawa, N.; Onose, Y.; Kimoto, K.; Zhang, W. Z.; Ishiwata, S.; Matsui, Y.; Tokura, Y. Near Room-Temperature Formation of a Skyrmion Crystal in Thin-Films of the Helimagnet Fege. *Nat. Mater.* **2011**, *10*, 106–109.

- (12) Wilhelm, H.; Baenitz, M.; Schmidt, M.; Rößler, U. K.; Leonov, A. A.; Bogdanov, A. N. Precursor Phenomena at the Magnetic Ordering of the Cubic Helimagnet FeGe. *Phys. Rev. Lett.* **2011**, *107*, 127203.
- (13) Seki, S.; Yu, X. Z.; Ishiwata, S.; Tokura, Y. Observation of Skyrmions in a Multiferroic Material. *Science* **2012**, *336*, 198–201.
- (14) Adams, T.; Chacon, A.; Wagner, M.; Bauer, A.; Brandl, G.; Pedersen, B.; Berger, H.; Lemmens, P.; Pfleiderer, C. Long-Wavelength Helimagnetic Order and Skyrmion Lattice Phase in Cu<sub>2</sub>OSeO<sub>3</sub>. *Phys. Rev. Lett.* **2012**, *108*, 237204.
- (15) Tonomura, A.; Yu, X.; Yanagisawa, K.; Matsuda, T.; Onose, Y.; Kanazawa, N.; Park, H. S.; Tokura, Y. Real-Space Observation of Skyrmion Lattice in Helimagnet MnSi Thin Samples. *Nano Lett.* **2012**, *12*, 1673–1677.
- (16) Milde, P.; Köhler, D.; Seidel, J.; Eng, L. M.; Bauer, A.; Chacon, A.; Kindervater, J.; Mühlbauer, S.; Pfleiderer, C.; Buhrandt, S.; et al. Unwinding of a Skyrmion Lattice by Magnetic Monopoles. *Science* **2013**, *340*, 1076–1080.
- (17) Wilson, M. N.; Karhu, E. A.; Quigley, A. S.; Rößler, U. K.; Butenko, A. B.; Bogdanov, A. N.; Robertson, M. D.; Monchesky, T. L. Extended Elliptic Skyrmion Gratings in Epitaxial MnSi Thin Films. *Phys. Rev. B: Condens. Matter Mater. Phys.* **2012**, *86*, 144420.
- (18) Wilson, M. N.; Butenko, A. B.; Bogdanov, A. N.; Monchesky, T. L. Chiral Skyrmions in Cubic Helimagnet Films: The Role of Uniaxial Anisotropy. *Phys. Rev. B: Condens. Matter Mater. Phys.* **2014**, *89*, 094411.
- (19) Yu, X. Z.; Onose, Y.; Kanazawa, N.; Park, J. H.; Han, J. H.; Matsui, Y.; Nagaosa, N.; Tokura, Y. Real-Space Observation of a Two-Dimensional Skyrmion Crystal. *Nature* **2010**, *465*, 901–904.
- (20) Park, H. S.; Yu, X.; Aizawa, S.; Tanigaki, T.; Akashi, T.; Takahashi, Y.; Matsuda, T.; Kanazawa, N.; Onose, Y.; Shindo, D.; et al. Observation of the Magnetic Flux and Three-Dimensional Structure of Skyrmion Lattices by Electron Holography. *Nat. Nanotechnol.* **2014**, *9*, 337–342.
- (21) Zhang, X. C.; Ezawa, M.; Zhou, Y. Magnetic Skyrmion Logic Gates: Conversion, Duplication and Merging of Skyrmions. *Sci. Rep.* **2015**, *5*, 9400.
- (22) Zhou, Y.; Ezawa, M. A Reversible Conversion between a Skyrmion and a Domain-Wall Pair in a Junction Geometry. *Nat. Commun.* **2014**, *5*, 4652.
- (23) Zhang, X. C.; Zhou, Y.; Ezawa, M.; Zhao, G. P.; Zhao, W. S. Magnetic Skyrmion Transistor: Skyrmion Motion in a Voltage-Gated Nanotrack. *Sci. Rep.* **2015**, *5*, 11369.
- (24) Fert, A.; Cros, V.; Sampaio, J. Skyrmions on the Track. *Nat. Nanotechnol.* **2013**, *8*, 152–156.
- (25) Widmann, S.; Günther, A.; Ruff, E.; Tsurkan, V.; Krug von Nidda, H.-A.; Lunkenheimer, P.; Loidl, A. Structural, Magnetic, Electric, Dielectric, and Thermodynamic Properties of Multiferroic GeV4s8. *Phys. Rev. B: Condens. Matter Mater. Phys.* **2016**, *94*, 214421.
- (26) Xu, K.; Xiang, H. J. Unusual Ferroelectricity Induced by the Jahn-Teller Effect: A Case Study on Lacunar Spinel Compounds. *Phys. Rev. B* **2015**, *92*, 121112.
- (27) Efthimiopoulos, I.; Khatri, I.; Liu, Z. T. Y.; Khare, S. V.; Sarin, P.; Tsurkan, V.; Loidl, A.; Zhang, D.; Wang, Y. Universal Link of Magnetic Exchange and Structural Behavior under Pressure in Chromium Spinels. *Phys. Rev. B: Condens. Matter Mater. Phys.* **2018**, *97*, 184435.
- (28) Efthimiopoulos, I.; Lochbiler, T.; Tsurkan, V.; Loidl, A.; Feleau, V.; Wang, Y. Structural Behavior of ZnCr<sub>2</sub>S<sub>4</sub> Spinel under Pressure. *J. Phys. Chem. C* **2017**, *121*, 769–777.
- (29) Ruiz-Fuertes, J.; Segura, A.; Rodriguez, F.; Errandonea, D.; Sanz-Ortiz, M. N. Anomalous High-Pressure Jahn-Teller Behavior in Cu<sub>2</sub>O<sub>4</sub>. *Phys. Rev. Lett.* **2012**, *108*, 166402.
- (30) Mokdad, J.; Knebel, G.; Marin, C.; Brison, J.-P.; Ta Phuoc, V.; Sopracase, R.; Colin, C.; Braithwaite, D. Structural, Magnetic, and Insulator-to-Metal Transitions under Pressure in the Gav4s8Mott Insulator: A Rich Phase Diagram up to 14.7 GPa. *Phys. Rev. B: Condens. Matter Mater. Phys.* **2019**, *100*, 245101.
- (31) Widmann, S.; Ruff, E.; Günther, A.; Krug von Nidda, H.-A.; Lunkenheimer, P.; Tsurkan, V.; Bordács, S.; Kézsmárki, I.; Loidl, A. On the Multiferroic Skyrmion-Host Gav4s8. *Philos. Mag.* **2017**, *97*, 3428–3445.
- (32) Mao, H. K.; Xu, J.; Bell, P. M. Calibration of the Ruby Pressure Gauge to 800 Kbar under Quasi-Hydrostatic Conditions. *J. Geophys. Res.* **1986**, *91*, 4673–4676.
- (33) Errandonea, D.; Boehler, R.; Japel, S.; Mezouar, M.; Benedetti, L. R. Structural Transformation of Compressed Solid Ar: An X-Ray Diffraction Study to 114gpa. *Phys. Rev. B: Condens. Matter Mater. Phys.* **2006**, *73*, 092106.
- (34) Klotz, S.; Chervin, J.-C.; Munsch, P.; Le Marchand, G. Hydrostatic Limits of 11 Pressure Transmitting Media. *J. Phys. D: Appl. Phys.* **2009**, *42*, 075413.
- (35) Rivers, M.; Prakapenka, V. B.; Kubo, A.; Pullins, C.; Holl, C. M.; Jacobsen, S. D. The Compres/Gsears Gas-Loading System for Diamond Anvil Cells at the Advanced Photon Source. *High Pressure Res.* **2008**, *28*, 273–292.
- (36) Prescher, C.; Prakapenka, V. B. Dioptas: A Program for Reduction of Two-Dimensional X-Ray Diffraction Data and Data Exploration. *High Pressure Res.* **2015**, *35*, 223–230.
- (37) Toby, B. H.; Von Dreele, R. B. Gsas-II: The Genesis of a Modern Open-Source All Purpose Crystallography Software Package. *J. Appl. Crystallogr.* **2013**, *46*, 544–549.
- (38) Vitalij, K. P.; Peter, Y. Z. *Fundamentals of Powder Diffraction and Structural Characterization of Materials*, 2nd ed.; Springer: New York, 2009.
- (39) Zhang, D.; Dera, P. K.; Eng, P. J.; Stubbs, J. E.; Zhang, J. S.; Prakapenka, V. B.; Rivers, M. L. High Pressure Single Crystal Diffraction at Px4.2. *J. Vis. Exp.* **2017**, *119*, 54660.
- (40) Dera, P.; Zhuravlev, K.; Prakapenka, V.; Rivers, M. L.; Finkelstein, G. J.; Grubor-Urosevic, O.; Tschauner, O.; Clark, S. M.; Downs, R. T. High Pressure Single-Crystal Micro X-Ray Diffraction Analysis with Gse\_Ada/Rsv Software. *High Pressure Res.* **2013**, *33*, 466–484.
- (41) Novak, G. A.; Colville, A. A. A Practical Interactive Least-Squares Cell-Parameter Program Using an Electronic Spreadsheet and a Personal Computer. *Am. Mineral.* **1989**, *74*, 488–490.
- (42) Momma, K.; Izumi, F. Vesta 3 for Three-Dimensional Visualization of Crystal, Volumetric and Morphology Data. *J. Appl. Crystallogr.* **2011**, *44*, 1272–1276.
- (43) Torikachvili, M. S.; Kim, S. K.; Colombier, E.; Bud'ko, S. L.; Canfield, P. C. Solidification and Loss of Hydrostaticity in Liquid Media Used for Pressure Measurements. *Rev. Sci. Instrum.* **2015**, *86*, 123904.
- (44) Klotz, S.; Chervin, J.-C.; Munsch, P.; Le Marchand, G. Hydrostatic Limits of 11 Pressure Transmitting Media. *J. Phys. D: Appl. Phys.* **2009**, *42*, 075413.
- (45) Errandonea, D.; Muñoz, A.; Gonzalez-Platas, J. Comment on “High-Pressure X-Ray Diffraction Study of Yb<sub>2</sub>O<sub>3</sub>/Eu<sup>3+</sup>, Gd<sub>2</sub>O<sub>3</sub>, and Eu<sub>2</sub>O<sub>3</sub>: Pressure-Induced Amorphization in Gd<sub>2</sub>O<sub>3</sub>. *J. Appl. Phys.* **2014**, *115*, 216101.
- (46) Li, M.; Gao, C.; Ma, Y.; Li, Y.; Li, X.; Li, H.; Liu, J.; Hao, A.; He, C.; Huang, X.; Zhang, D.; Yu, C. New Diamond Anvil Cell System for in Situ Resistance Measurement under Extreme Conditions. *Rev. Sci. Instrum.* **2006**, *77*, 123902.
- (47) Errandonea, D.; Segura, A.; Martínez-García, D.; Muñoz-San Jose, V. Hall-Effect and Resistivity Measurements in CdTe and ZnTe at High Pressure: Electronic Structure of Impurities in the Zinc-Blende Phase and the Semimetallic or Metallic Character of the High-Pressure Phases. *Phys. Rev. B: Condens. Matter Mater. Phys.* **2009**, *79*, 125203.
- (48) Birch, F. Finite Elastic Strain of Cubic Crystals. *Phys. Rev.* **1947**, *71*, 809–824.
- (49) Murnaghan, F. D. The Compressibility of Media under Extreme Pressure. *Proc. Natl. Acad. Sci. U. S. A.* **1944**, *30*, 244–247.
- (50) Errandonea, D.; Kumar, R. S.; Manjón, F. J.; Ursaki, V. V.; Rusu, E. V. Post-Spinel Transformations and Equation of State in ZnGa<sub>2</sub>O<sub>4</sub>: Determination at High Pressure by in Situ X-Ray

Diffraction. *Phys. Rev. B: Condens. Matter Mater. Phys.* **2009**, *79*, 024103.

(51) Efthimiopoulos, I.; Liu, Z. T. Y.; Khare, S. V.; Sarin, P.; Tsurkan, V.; Loidl, A.; Popov, D.; Wang, Y. Structural Transition in the Magnetoelectric ZnCr<sub>2</sub>Se<sub>4</sub> Spinel under Pressure. *Phys. Rev. B: Condens. Matter Mater. Phys.* **2016**, *93*, 174103.

(52) Efthimiopoulos, I.; Liu, Z. T. Y.; Khare, S. V.; Sarin, P.; Lochbiler, T.; Tsurkan, V.; Loidl, A.; Popov, D.; Wang, Y. Pressure-Induced Transition in the Multiferroic CoCr<sub>2</sub>O<sub>4</sub> Spinel. *Phys. Rev. B: Condens. Matter Mater. Phys.* **2015**, *92*, 064108.

(53) Efthimiopoulos, I.; Tsurkan, V.; Loidl, A.; Zhang, D.; Wang, Y. Comparing the Pressure-Induced Structural Behavior of CuCr<sub>2</sub>O<sub>4</sub> and CuCr<sub>2</sub>Se<sub>4</sub> Spinels. *J. Phys. Chem. C* **2017**, *121*, 16513–16520.

(54) Efthimiopoulos, I.; Liu, Z. T. Y.; Kucway, M.; Khare, S. V.; Sarin, P.; Tsurkan, V.; Loidl, A.; Wang, Y. Pressure-Induced Phase Transitions in the CdCr<sub>2</sub>Se<sub>4</sub> Spinel. *Phys. Rev. B: Condens. Matter Mater. Phys.* **2016**, *94*, 174106.

(55) Hlinka, J.; Borodavka, F.; Rafalovskyi, I.; Docekalova, Z.; Pokorný, J.; Gregora, I.; Tsurkan, V.; Nakamura, H.; Mayr, F.; Kuntscher, C. A.; et al. Lattice Modes and the Jahn-Teller Ferroelectric Transition of Gav<sub>4</sub>s<sub>8</sub>. *Phys. Rev. B* **2016**, *94*, 060104.

(56) Errandonea, D.; Manjón, F. J. On the Ferroelastic Nature of the Scheelite-to-Fergusonite Phase Transition in Orthotungstates and Orthomolybdates. *Mater. Res. Bull.* **2009**, *44*, na.

(57) Abd-Elmeguid, M. M.; Ni, B.; Khomskii, D. I.; Pocha, R.; Johrendt, D.; Wang, X.; Syassen, K. Transition from Mott Insulator to Superconductor in Ganb<sub>4</sub>se<sub>8</sub> and Gata<sub>4</sub>se<sub>8</sub> under High Pressure. *Phys. Rev. Lett.* **2004**, *93*, 126403.

(58) Saccone, F. D.; Ferrari, S.; Errandonea, D.; Grinblat, F.; Biloval, V.; Agouram, S. Cobalt Ferrite Nanoparticles under High Pressure. *J. Appl. Phys.* **2015**, *118*, 075903.

(59) Saqib, H.; Rahman, S.; Errandonea, D.; Susilo, R. A.; Jorge-Montero, A.; Rodriguez-Hernandez, P.; Munoz, A.; Sun, Y.; Chen, Z.; Dai, N.; Chen, B.; et al. Giant Conductivity Enhancement: Pressure-Induced Semiconductor-Metal Phase Transition in Cd<sub>0.90</sub>n<sub>0.1</sub>Te. *Phys. Rev. B: Condens. Matter Mater. Phys.* **2019**, *99*, 094109.